

# Supplement: Near-field Infrared Vibrational Dynamics and Tip-Enhanced Decoherence

Xiaoji G. Xu, and Markus B. Raschke\*

*Department of Physics, Department of Chemistry, and JILA, University of Colorado, Boulder, CO  
80309, United States*

E-mail: markus.raschke@colorado.edu

## Vibrational near-field response

In addition to the study of the symmetric resonance  $\nu_1 = 1160 \text{ cm}^{-1}$  of PTFE as discussed in the main text, we have also investigated the anti-symmetric resonance  $\nu_2 = 1220 \text{ cm}^{-1}$ . It exhibits corresponding free induction decay behavior in the interferogram and characteristic spectral signatures in the Fourier transform.

Figure S1 shows the fs *s*-SNOM results for  $\nu_2$  with the central frequency of the mid-IR pump tuned to the  $\nu_2$  spectral position. Figure S1 a) shows the near-field interferogram at the second harmonic demodulation ( $2\Omega$ ) with FID behavior (blue curve) in comparison with the envelope of the laser interferogram (red dashed curve). The amplitudes of the corresponding Fourier transforms are shown in Figure S1 b). The spectral phase is shown in Figure S1 c) (blue curve) with FTIR absorption spectrum (black dashed curve) as reference. Despite the low spectral laser power around  $1160 \text{ cm}^{-1}$ , the spectral phase clearly reveals also the presence of  $\nu_1$ . Figure S1 d) and e) show the corresponding short-time Fourier transform spectrograms of the pump pulse interferogram (d)

---

\*To whom correspondence should be addressed

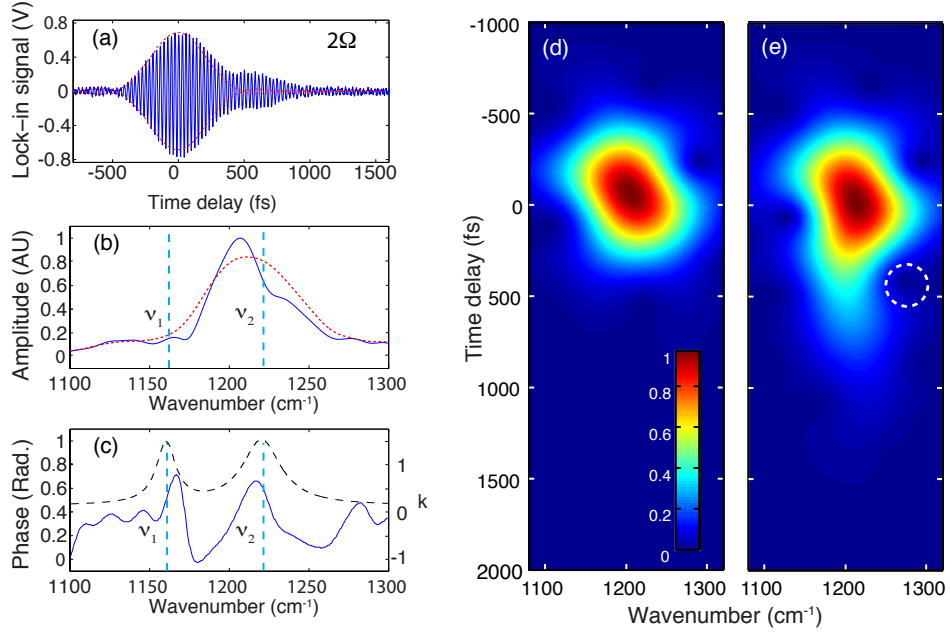


Figure S1: Near-field  $s$ -SNOM interferogram of PTFE at the  $\nu_2$  resonance (a, blue trace) with laser spectrum centered at  $1220 \text{ cm}^{-1}$ , with laser interferogram envelope shown as reference (red dashed line). Corresponding Fourier transforms are shown in (b). Spectral phase (c, dashed curve) with absorption profile (black dashed curve) for comparison. Short-time Fourier transform spectrograms of the laser pulse (d) and PTFE  $s$ -SNOM (e) represent the details of the spectro-temporal evolution of the radiative free-induction decay of the underlying  $\nu_2$  C – F resonance. A 200 fs Gaussian width function is used in the short-time Fourier transform.

and the near-field scattering interferogram of PTFE (e), respectively. Note the effect of the shorter far-field dephasing time  $T_2^{FF}$  of  $\sim 340$  fs for  $\nu_2$  compared to  $\sim 680$  fs for  $\nu_1$ .

## Near-field vertical and lateral spatial localization

The spatial near-field localization is determined by the geometry of the tip apex. Figure S2 a) shows a tip-sample approach curve (square symbols) on PTFE that illustrates the near-field interaction range. It is recorded at the second-harmonic lock-in demodulation without interferometric heterodyne amplification (i.e., spectrally integrated). Figure S2 b) illustrates the increase in near-field localization with increasing harmonics as a result of the nonlinear tip-sample coupling. The approach curves shown are measured on the gold surface as reference. The gold surface is used to

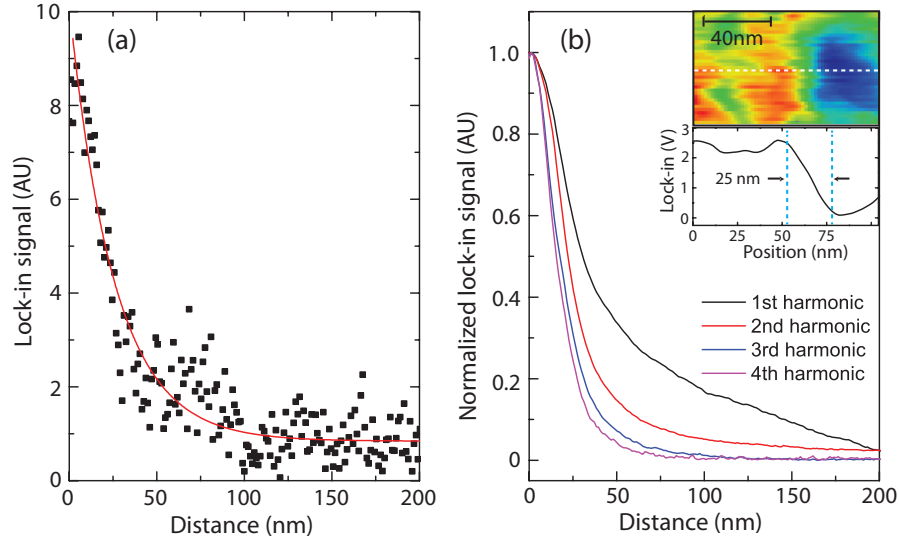


Figure S2: Spectrally integrated tip-sample *s*-SNOM distance dependence on PTFE (a, with red line as guide to the eye) from second harmonic lock-in demodulation ( $2\Omega$ ). For comparison, a set of approach curves (b) from 1st to 4th harmonics for a gold surface (intensities normalized). Inset: *s*-SNOM image of gold surface feature with lateral signal variation corresponding to vertical near-field localization and apex radius.

provide higher signal strength under otherwise identical experimental conditions. The correlation of vertical near-field localization with lateral resolution and the tip radius (ca. 25 nm in this case) can be seen from the *s*-SNOM scan of a surface feature (b, inset) and corresponding line cut (dotted white line).

## Interferogram envelope progression with lock-in demodulation harmonics

Our experimental setup allows for the simultaneous recording of multiple interferograms for each lock-in harmonic. The measured *s*-SNOM interferograms from the first four harmonics ( $\Omega$ ,  $2\Omega$ ,  $3\Omega$ , and  $4\Omega$ ) with the tip engaged in non-contact mode feedback with the PTFE sample are shown in Figure S3 (a-d, blue trace). The envelope of the corresponding signal acquired for a gold surface under otherwise identical experimental conditions is shown (red dashed) as reference. Correspond-

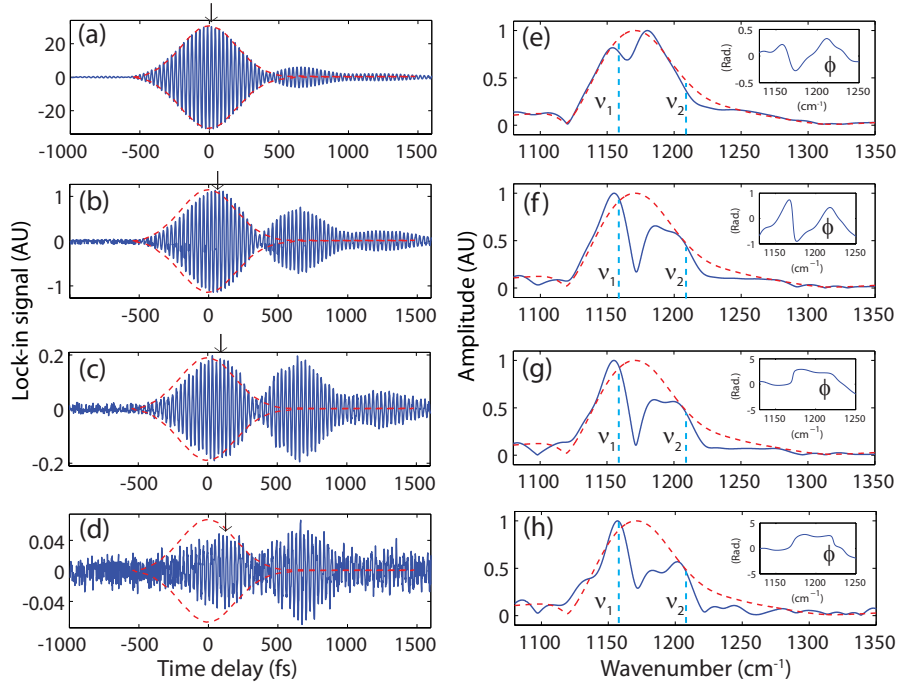


Figure S3: Progression of non-resonant near-field and far-field background with increase in resonant near-field free induction decay contrast with increasing detection harmonics (a-d, with increasing harmonics from  $\Omega$  to  $4\Omega$ ). Envelope of pump pulse interferogram (red dashed). Corresponding Fourier transforms (e-h) with laser spectrum (red dashed line) as reference, shows the underlying FID vibrational resonances, and a phase related dispersive profile. Insets: corresponding spectral phase behavior.

ing Fourier transforms are shown in Figure S3 (e-h, blue) with excitation pulse spectra (red dashed). There is a general decrease in *s*-SNOM intensity with increasing harmonics. The relative far-field contribution decreases more rapidly than the near-field signal contribution with higher lock-in harmonic demodulation. As a result, a general increase in the relative intensity of the FID tail with respect to the pulse overlap intensity can be observed. At larger time delays ( $>650$  fs), the tails of the four demodulation FID interferograms are very similar, albeit with a decrease in signal to noise ratios due to a decrease of the absolute signal level. Spectral phases from each lock-in harmonic are shown in the insets of Figure S3 e-h).

Figure S4 a) shows the resulting intensity ratios between the FID tail (represented by the maxima of second envelope around 650 fs) and the envelope maximum of first lobe immediately after time zero. The destructive interference between far-field scattering and resonant near-field scatter-

ing leads to a delayed rise of the signal maxima of the first lobe (marked by arrows in Figure S3 a-d). The positions of the maxima of the initial pulse overlap are plotted in Figure S4 b). Such a delayed rise can be attributed to the destructive interference between the far-field and near-field signal contributions, as with higher harmonic demodulation the near-field to far-field contrast increases.

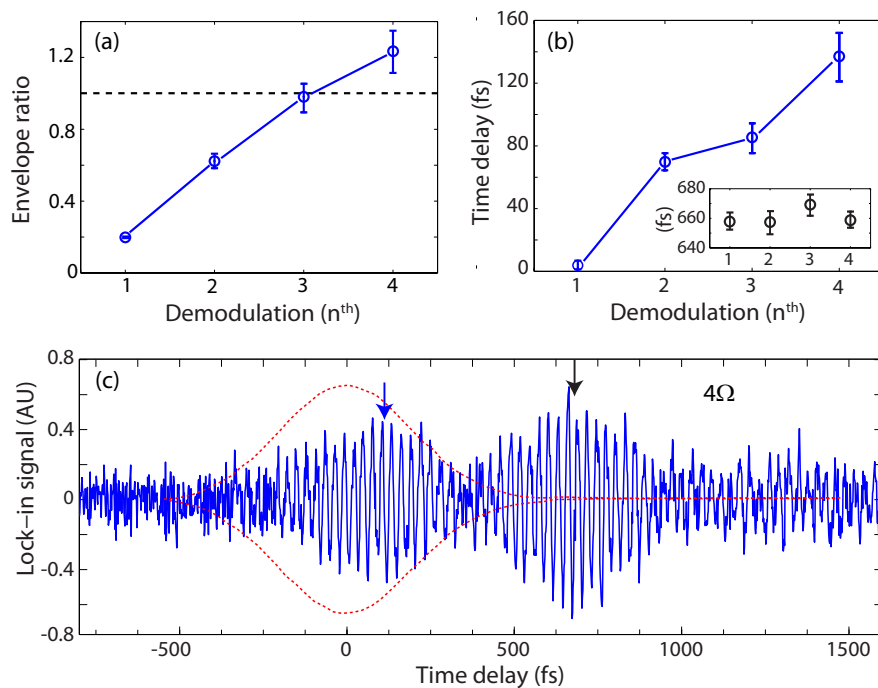


Figure S4: Intensity ratios between the second interferogram maximum and the initial lobe intensity maximum from the first to the fourth lock-in demodulations (a). Increasing delay of the envelope maximum of the first lobe with higher lock-in demodulation is observed (b), whereas the position of the second maximum is rather constant (inset). The near-field interferogram from lock-in  $4\Omega$  demodulation (c, blue) and laser interferometric envelope (c, red dashed). Note that the intensity of the second maximum is higher than the first maximum.

A notable phenomenon is seen in the FID interferogram of the fourth-harmonic signal (see Figure S4 c). The height of the first lobe envelope (marked by blue arrow) is slightly lower than the subsequent second maximum (marked by black arrow). For typical FID measurements, the excitation period of the vibrational oscillator ensemble is followed by a continuous decrease of the amplitude of the envelope starting from the maximum value after the initial induction period. Such observation of a FID with a larger tail than the initial “induction” intensity is unusual. In an absorptive type of asymmetric heterodyne interferogram, the frequency components that have

been absorbed also create a FID tail. In this case, the second lobe of such FID tail should always be smaller than the first one. In contrast, in an emission type heterodyne interferogram, such as photon echo or ultrafast wave mixing, the destructive interference between modes can in principle reduce the first lobe of a heterodyne interferogram. Given the fact that the fourth harmonic extracts primarily near-field components, the observation of a reduction of the first lobe height below the height of the second lobe indicates the emission attribute of the near-field response, and possible destructive interference between resonant and non-resonant near-field polarization contributions.

## Model calculation

The underlying physics that describes the optical tip-sample interaction is qualitatively well captured by the simple dipole-dipole model used to describe *s*-SNOM.<sup>1,2</sup> Here the tip is treated as a small polarizable sphere in the quasi-static limit ( $d \ll \lambda$ ) with its image dipole reflecting the local material dielectric function and its resonances. With both real and imaginary part of the dielectric function contributing to the *s*-SNOM response this gives rise to the spectral phase behavior observed. Furthermore, the tip locally increases the field strength of the driving field and induced resonant polarization. In the time domain interpretation, the tip dipole acquires far-field excitation energy and drives the molecules in the sample coherently with increasing efficiency depending on the near-field coupling. Finite damping on resonance then leads to the observed prolonged time domain behavior in the interferograms with characteristic decoherence time  $T_2$  related to the FWHM line width  $\Gamma = 1/T_2$ . The duration of the prolonged time domain behavior is determined by the dielectric function of the sample if the tip is non-resonant.

Following the established procedure<sup>1,2</sup> the polarizability  $\alpha$  of the tip as a function of the dielectric function of the tip material  $\epsilon_t(\omega)$  is approximated by the response of the sphere as:

$$\alpha = 4\pi r^3 \frac{\epsilon_t(\omega) - 1}{\epsilon_t(\omega) + 2}, \quad (1)$$

with  $r$  being the tip radius. The total effective polarizability of the near-field coupled tip and sample

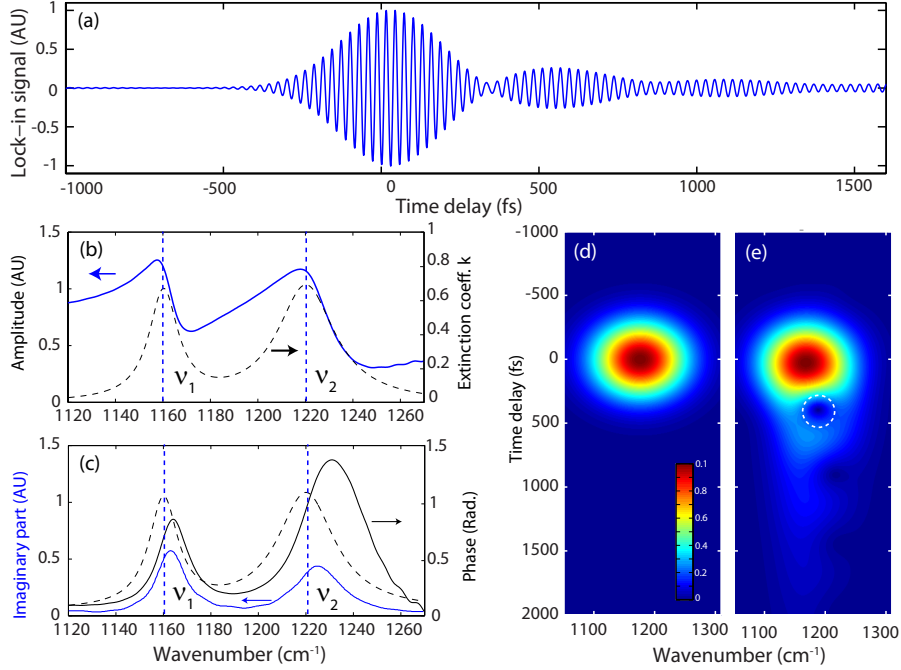


Figure S5: Numeric simulation of the free induction decay interferogram based on PTFE spectroscopic data (a) with excitation frequency centered at  $1170 \text{ cm}^{-1}$ . Corresponding Fourier transform with amplitude (b, blue), spectral phase (c, blue), imaginary part (c, black), and PTFE absorption spectrum (b,c, black dashed). Short-time Fourier transform spectrogram of the laser (d) and the spectrogram of the near-field FID interferogram of (a) is shown in (e). Beating behavior at the blue side of interferogram and a characteristic interference dip (dashed circle), similar to observations in spectrogram reconstruction of the experimental interferogram in Figure 4) of the main article.

system (image dipole) is then described by:

$$\alpha_{\text{eff}}(\omega) = \alpha \left( 1 - \frac{\alpha\beta}{16\pi(r+z)^3} \right)^{-1} \quad (2)$$

with  $z$  being the tip sample distance.<sup>1</sup> The term  $\beta(\omega) = (\varepsilon(\omega) - 1)/(\varepsilon(\omega) + 1)$  carries the dependence on the sample dielectric function  $\varepsilon(\omega)$  with its vibrational resonances.  $\varepsilon(\omega)$  is related to the complex refractive index by  $\varepsilon(\omega) = (n + ik)^2$ . Assuming a broad spectral width for the excitation field  $E(\omega)$ , the scattered tip-sample near field is then given by  $E_s(\omega) = \alpha_{\text{eff}}(\omega)E(\omega)$  in the frequency domain. Considering the effect of far-field background, the total scattered light field is given by  $E_{\text{total}}(\omega) = \alpha_{\text{eff}}(\omega)E(\omega) + b(z)E(\omega)e^{i\phi}$  with  $b(z)$  and  $\phi$  being the apex position dependent amplitude and phase difference between near-field signal and far-field scattering

respectively. The heterodyne detection is achieved by interference of all scattered light fields in  $E_{total}(\omega)$ , with a time delayed reference pulse given by  $E(\omega)e^{-i\omega\tau}$  in the frequency domain. The interferogram can then be obtained by varying the time delay  $\tau$  and integrating the intensity of the heterodyned signal over frequency. Figure S5 a) shows the resulting simulated interferogram based on the spectroscopic PTFE data from literature.<sup>3</sup>

The model qualitatively reproduces the shape of the asymmetric FID interferogram. In agreement with the experiment, the destructive interference between the far-field and near-field signal contributions gives rise to the signal dip at the end of the driving laser pulse. The subsequent beating is due to the interference between  $\nu_1$  and  $\nu_2$ , and primarily dominated by  $\nu_1$  at later time delays.

The spectral amplitude (b) and phase (c) are obtained following the same procedure as in the experiment, here applied to the calculated interferogram (a). The spectral amplitude has the dispersive profile as expected and as also observed in the experiment. The normalized spectral phase (c, black solid curve) resembles the spectral profile of the extinction coefficient (dashed curve), but with a notable blue shift due to the tip-sample coupling.

With all parameters well defined, the imaginary part of near-field response can be derived without ambiguities (Figure S5 c, blue solid line). It better resembles the absorption profile as expected, albeit still exhibits a distinct blue shift due to the tip-sample coupling.

## References

- (1) Raschke, M. B.; Lienau, C. *Applied Physics Letters* **2003**, *83*, 5089–5091.
- (2) Keilmann, F.; Hillenbrand, R. *Philosophical Transactions of the Royal Society of London Series a-Mathematical Physical and Engineering Sciences* **2004**, *362*, 787–805.
- (3) Korte, E. H.; Roseler, A. *Analytical and Bioanalytical Chemistry* **2005**, *382*, 1987–1992.